Vortex method for simulation of a 3D round jet in a cross-stream

Grégory Pinon, H. Bratec, S. Huberson, G. Pignot, E. Rivoalen

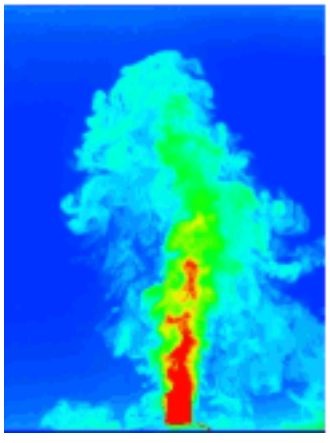

Journal of Turbulence
Publication details, including instructions for authors and subscription information:
http://www.tandfonline.com/loi/tjot20

Vortex method for simulation of a 3D round jet in a cross-stream

G. Pinon [a], H. Bratec [a], S. Huberson [a], G. Pignot [a] & E. Rivoalen [a]

[a] Université du Havre, 25 rue Philippe Lebon, BP 540, 76058, Le Havre Cedex, France

Published online: 04 Oct 2011.

To cite this article: G. Pinon, H. Bratec, S. Huberson, G. Pignot & E. Rivoalen (2005) Vortex method for simulation of a 3D round jet in a cross-stream, Journal of Turbulence, 6, N18, DOI: 10.1080/14685240500209981

To link to this article: http://dx.doi.org/10.1080/14685240500209981

Journal of Turbulence
Volume 6, No. 18, 2005

Vortex method for simulation of a 3D round jet in a cross-stream

G. PINON*, H. BRATEC, S. HUBERSON, G. PIGNOT and E. RIVOALEN

Université du Havre, 25 rue Philippe Lebon, BP 540, 76058 Le Havre Cedex, France

In this paper, the three-dimensional (3D) flow of a jet in a crossflow was investigated. This is a numerical study based on a vortex particle method. In order to account for the lower length scales, a crude LES turbulence model was implemented together with a regridding procedure. The numerical simulation was done with an injection ratio $R_{\text{inj}} = W_{\text{jet}}/U_\infty = 4.0$. The code was run until an averaged steady state of the jet was reached. The resulting vortex structures were shown to be consistent with previously published analyses of the flow, from both experiments and numerical simulations. In particular, the onset of counter-rotating vortex pairs (CVP) was also investigated.

1. Introduction

Jets in crossflow are commonly encountered in a large part of engineering sciences, and technological applications are numerous, such as chimney flow for dispersion of pollutant, V/STOL aircraft aerodynamics, mixing devices, or even fuel or air injection in gas turbine engines.

Simulation of a three-dimensional (3D) jet is not a recent challenge in the computing sciences. Many authors have simulated 3D jets, either free jets or jets in crossflow, using various numerical methods, finite differences, finite volumes with RANS, LES, or DNS, and also Lagrangian-based methods. Boersma *et al*. [1] computed the DNS of round free jets for a low Reynolds number $Re = 2300$ in order to compare velocity profiles and turbulence intensities with the literature. Grinstein [2] and Grinstein and Devore [3], among others, have performed several LES compressible simulations with different types of nozzles: round nozzle, square nozzle, etc. Grinstein also focused on reactive jets and flame. Bogey *et al*. [4, 5] simulated 3D jets using LES, and Rembold *et al*. [6] simulated 3D jets using RANS, LES, and DNS, principally in order to predict the noise emission. In these simulations, turbulence was of great interest for its impact on the noise generated. Lighthill's approximation was used by Bogey and Rembold.

For jets in crossflow, simulations are more scarce. Among them, the LES simulation of Yuan *et al*. [7, 8] is noteworthy; Yuan *et al*. [7, 8] should be especially noted for their work on trajectories, entrainment, and identification of vortical structures. Some LES computations have also been done recently by Priere *et al.* [9], who studied the efficiency of a mixing device formed with rows of jets in crossflow. Cortelezzi and Karagozian [10] simulated a 3D round jet in crossflow with vortex methods in the vortex filaments version. However, they made the

*Corresponding author.

Journal of Turbulence
ISSN: 1468-5248 (online only) © 2005 Taylor & Francis
http://www.tandf.co.uk/journals
DOI: 10.1080/14685240500209981

restrictive assumption that all the vortex elements issuing from the nozzle's exit were linked to a vortex ring and that the fluid was inviscid. This means that the vortex elements are compelled to remain within the same vortex ring, and the method was apparently not able to deal with vortex breakdown.

Our simulation was based on vortex particles. One of the main advantages of this method is that the particles or blobs do not have any explicit geometrical connection, which enabled the simulation to treat such complicated situations as vortex breakdown or vortex merging.

With respect to the experimental point of view, references are rather numerous. Among the first measurements, of note are the papers by Keffer and Baines [11], Kamotani and Greber [12]. and Chassaing *et al*. [13], who performed important investigations concerning velocity and turbulence measurements using a hot-wire probe on round turbulent jets in crossflow. Moussa *et al*. [14] performed a substantial study of a jet in crossflow considering mean velocity profiles and vorticity contours. An interesting point of this work is the use of jets issuing from a pipe, as opposed to the former studies, which used flush-mounted nozzles. Then Crabb *et al*. [15] performed Laser–Doppler anemometry coupled with hot-wire measurements on round turbulent jets in crossflow with a relatively low injection ratio $R_{\text{inj}} = W_{\text{jet}}/U_{\infty}$ equal to 1.15 and 2.3.

More recently, a large part of the experimental studies on jets in crossflow were dedicated to the understanding of vortical structures both in the near field and in the far field [16, 17, 18]. Besides these, more advanced velocity measurement techniques were applied to free jets [19–23] as well as jets in crossflow with rectangular nozzle [24–26], shedding new light on the unsteady flow structure. In a recent experimental study, Lim *et al*. [27] focused on the vortical structures in the near field of a round free jet in crossflow. They suggested an alternative explanation for the onset of the counter-rotating vortex pair (CVP). This is one of the aspects that will be examined in this paper.

This article is divided into three main parts. First, we introduce the numerical method, which is a vortex method and explain how the particles are emitted from the pipe, as well as some other numerical aspects. In the second part, we present some results concerning the particles themselves and velocity characteristics. The last part is devoted to the vortical structure of the jet, and previous explanations concerning the dynamics of these structures will be examined.

2. Aspects of the numerical method

2.1 *Summary of the vortex method*

The first attempt of vortex method simulation was performed by Rosenhead [28] back in 1931. These first simulations became very well known, and since then, many authors have expanded the method, even to 3D cases. Rehbach [29] and later Leonard [30] set the principles of the method in three dimension. This is a Lagrangian-based method, well suited for the simulation of unsteady flow in an unbounded space, which is the case of jets, either free jets or jets in crossflow.

As in the primary cases of Rosenhead, the flow field is discretized with vortex blobs issuing from the edge of a pipe. The main advantage is that the blobs will only exist where the vorticity is not close to zero, which is a relatively concentrated zone. This will generate a rather low-cost simulation, even for very long simulations or very extended spaces. Concerning the blobs, emission, an approximated Kutta–Joukovsky condition was used to evaluate the amount of vorticity that had to be injected in the flow. In addition, a viscous and a turbulent diffusion model were added to the simulation. The turbulent diffusion model was developed by Mansour *et al*. [31], and is based on enstrophy. A global remeshing of the flow field was also performed to avoid the simulation collapsing.

2.1.1 Continuous formulation. We started with the Navier–Stokes equation for incompressible flow. Taking the curl of this equation, the pressure term disappears and we obtain the Navier–Stokes equation in $(\boldsymbol{\omega}, \boldsymbol{U})$ formulation with $\boldsymbol{\omega} = \nabla \wedge \boldsymbol{U}$ the vorticity field of the flow.

$$\begin{cases} \nabla \cdot \boldsymbol{U} = 0, \qquad \nabla \wedge \boldsymbol{U} = \boldsymbol{\omega} & \text{(1a)} \\ \dfrac{D\boldsymbol{\omega}}{Dt} = (\boldsymbol{\omega} \cdot \nabla)\boldsymbol{U} + \nu \triangle \boldsymbol{\omega} & \text{(1b)} \end{cases}$$

$D\boldsymbol{\omega}/Dt$ is the material derivative and $\boldsymbol{U}$ the velocity component. In this paper, bold symbols refer to vectors, and we will denote, for instance, v the Euclidian norm of any vector $\boldsymbol{v}$.

Equation (1b) is the starting point for the vortex method. This is basically the transport equation of $\boldsymbol{\omega}$, the quantity carried in the blobs. $D\boldsymbol{\omega}/Dt$ represents the transport term in a Lagrangian frame, $(\boldsymbol{\omega}.\nabla)\boldsymbol{U}$ stands for the stretching term, which disappears in two dimensions, and $\nu \triangle \boldsymbol{\omega}$ accounts for diffusion. The Helmholtz decomposition of the velocity, equation (2),

$$\boldsymbol{U} = \nabla \wedge \boldsymbol{\psi} + \nabla \phi \tag{2}$$

together with equations (1a) yields:

$$\triangle \phi = 0 \tag{3a}$$

and

$$\triangle \boldsymbol{\psi} = -\boldsymbol{\omega} \tag{3b}$$

Assuming that the vorticity field is known, the rotational component of the velocity field $\boldsymbol{U}_\omega$ is readily obtained, thanks to the Poisson equation (3b) and the Biot–Savart relation, equation (4b):

$$\boldsymbol{K}(\boldsymbol{r}) = \frac{\boldsymbol{r}}{r^3} \tag{4a}$$

and

$$\boldsymbol{U}_\omega(\boldsymbol{r}) = \frac{1}{4\pi} \int_{\mathcal{V}} \boldsymbol{K}(\boldsymbol{r} - \boldsymbol{r}') \wedge \boldsymbol{\omega}(\boldsymbol{r}') dv' \tag{4b}$$

The velocity potential ϕ is defined thanks to $\boldsymbol{U}_\omega$ and the boundary conditions (see section 2.2).

2.1.2 Discrete formulation. In this sub-section, only the Euler equation is considered. The diffusive part of the previous equation (1b) will be dealt with in section 2.3 in order to provide a complete discretization of the Navier–Stokes equation.

The first step is to discretize the vorticity field into vortex elements, which are termed either blobs or particles indifferently hereafter. Then, in a second step, these particles are advected thanks to the velocity field calculated as defined in equation (7). In order to define the position of the particles, dv is assumed to be a small volume whose support is $\mathcal{P}_i$. The position $\boldsymbol{X}_i$ of the particle i is defined by equation (5a), and the vorticity $\boldsymbol{\Omega}_i$ carried by this particle by equation (5b).

$$\boldsymbol{X}_i = \frac{\int_{\mathcal{P}_i} \boldsymbol{x} dv}{\int_{\mathcal{P}_i} dv} \tag{5a}$$

$$\boldsymbol{\Omega}_i = \int_{\mathcal{P}_i} \boldsymbol{\omega} dv \tag{5b}$$

After a few mathematical manipulations, and assuming that $\boldsymbol{U}_i = \boldsymbol{U}(\boldsymbol{X}_i)$ is the velocity of the ith blob, these last definitions lead to the following equations:

$$\begin{cases} \dfrac{d\boldsymbol{X}_i}{dt} = \boldsymbol{U}_i & \text{(6a)} \\ \dfrac{d\boldsymbol{\Omega}_i}{dt} = (\boldsymbol{\Omega_i}.\nabla)\boldsymbol{U_i} & \text{(6b)} \end{cases}$$

At this point, it has to be mentioned that the velocity $\boldsymbol{U}$ is not only made up by the rotational component $\boldsymbol{U}_\omega$. In fact, two other terms denoted $\boldsymbol{U}_\phi$ and $\boldsymbol{U}_s$ need to be added to $\boldsymbol{U}_\omega$ in order to account for the pipe wall and the inflow, respectively. The general form of the velocity $\boldsymbol{U}$ is then the sum of these three components, as equation (13) explains.

As usual, owing to the singular behaviour of the Green kernel, a regularized kernel $\boldsymbol{K}_\delta$ has to be used in the discrete Biot–Savart law, yielding:

$$\boldsymbol{K}_\delta(\boldsymbol{r}) = \frac{\boldsymbol{r}}{(r^6 + \delta^6)^{\frac{1}{2}}} \tag{7a}$$

and

$$\boldsymbol{U}_{\omega_i} = \frac{1}{4\pi} \sum_{j=1}^{N_\Omega} \boldsymbol{K}_\delta(\boldsymbol{X}_i - \boldsymbol{X}_j) \wedge \boldsymbol{\Omega}_j \tag{7b}$$

In order to avoid collapse of the calculation, a global regridding of the particles was also included every four time steps. This regridding used the interpolation formula M_4'. It is clear that remeshing alters the accuracy of the calculation, although it can be kept within a very reasonable range. A more complete survey of the effect of global remeshing is available in the references [32 and 33], where different interpolation formulae have been studied in terms of the L_2 velocity error introduced in the simulation. These studies concluded that the third-order interpolation formula M_4' provides a good compromise between accuracy, smoothness of the results, and implementation's work. Among the numerical aspects treated in this section is also the integration scheme. A second-order Runge–Kutta was used as the time integration scheme for these simulations in order to obtain a good compromise between accuracy and time saving.

2.2 *Flow generation and pipe influence*

Particles were generated at every time step at the pipe exit, and the quantity of vorticity that had to be introduced in the blobs was calculated with a Kutta–Joukovsky condition (see section 2.3). In order to generate the velocity, a source point P_Q^o with intensity Q was located inside the discretized pipe portion and generated the flow. The velocity component resulting from the presence of this point source was evaluated with equation (8). The current configuration is rather similar to the one used by Nitsche [34] in her axisymmetrical computations.

$$\boldsymbol{U}_s = \frac{Q}{4\pi} \frac{\boldsymbol{r}}{r^3} \tag{8}$$

The quantity Q was evaluated every time step so that the desired velocity at the pipe exit was obtained. In practice, the source point P_Q^o was associated with a control point P_Q^c, located at the centre of the pipe exit section [see figure (2)], where an estimated velocity was imposed and the source intensity computed accordingly.

The pipe was accounted for with a boundary integral equation, which enabled the imposition of the desired slip condition onto the pipe wall. The pipe wall (S) was discretized into N_p

surface elements, $N_p = 1800$ for this simulation. Each surface element had a normal unit vector $\boldsymbol{n}$ and a surface ds, P being a control point located at the centre of the considered surface element. Letting ϕ be the velocity potential induced by these boundary elements, ϕ is harmonic ($\triangle\phi = 0$) owing to the divergence free of the flow field, equations (1a) and (3a). The slip condition was imposed at every control point P of the pipe surface (S), and ϕ must satisfy equations (9a and 9b):

$$\begin{cases} \dfrac{\partial \phi}{\partial \boldsymbol{n}} = -\boldsymbol{V} \cdot \boldsymbol{n} \quad (S) & \text{(9a)} \\ lim_{\boldsymbol{r}\to\infty} \nabla\phi = 0 & \text{(9b)} \end{cases}$$

where $\boldsymbol{V}$ is the sum of the both contribution, $\boldsymbol{U}_s(P)$ owing to the source Q and $\boldsymbol{U}_\omega(P)$ owing to the presence of the particles.

M being any point of the flow field, a solution for the potential function ϕ was obtained with the third Green's relation:

$$\phi(M) = \frac{1}{4\pi} \int \int_S \mu(P) \frac{\boldsymbol{MP}.\boldsymbol{n}(P)}{MP^3} ds \tag{10}$$

where $\mu(P)$ represents a distribution of normal doublet on the pipe surface (S). The velocity component $\boldsymbol{U}_\phi$, which is derived from the potential ϕ, is basically the gradient of ϕ. Taking into account that the surface is discretized into surface elements of area ds_p and assuming that the doublet distribution $\mu(P)$ is constant on a surface element and equal to μ_p, the velocity component $\boldsymbol{U}_\phi$ is expressed by equation (11).

$$\boldsymbol{U}_\phi = \frac{1}{4\pi} \sum_{p=1}^{Np} \mu_p \nabla \left(\frac{\boldsymbol{MP}.\boldsymbol{n}_p}{MP^3} \right) ds_p \tag{11}$$

Finally, the presence of the pipe and the generation of the flow resulting from the point source can be included in a matrix in order to enforce all these conditions at the same time. This matrix has the following form:

$$\begin{bmatrix} a_{P_1P_1} & & a_{P_1P_{N_p}} & d_{P_1P_Q^o} \\ & \cdots & & \\ a_{P_{N_p}P_1} & & a_{P_{N_p}P_{N_p}} & d_{P_{N_p}P_Q^o} \\ c_{P_Q^cP_1} & & c_{P_Q^cP_{N_p}} & b_{P_Q^cP_Q^o} \end{bmatrix} \begin{bmatrix} \mu_1 \\ \cdots \\ \mu_{N_p} \\ Q \end{bmatrix} = \begin{bmatrix} -\boldsymbol{V}_{P_1}.\boldsymbol{n}_{P_1} \\ \\ -\boldsymbol{V}_{P_{N_p}}.\boldsymbol{n}_{N_p} \\ -\boldsymbol{V}_{P_Q^c}.\boldsymbol{n}_{P_Q^c} \end{bmatrix} \tag{12}$$

where a_{ij} is the influence of the unitary normal doublet of the j^{th} surface element onto the i^{th} one, $b_{P_Q^cP_Q^o}$ the influence of the point source P_Q^o onto the point control P_Q^c associated with the source Q, $c_{P_Q^cj}$ the influence of the jth unitary normal doublet of the pipe onto the point control P_Q^c, and $d_{iP_Q^o}$ stands for the influence owing to the point source P_Q^o onto the ith discrete element of the pipe. As the pipe is fixed, and the source and control points do not change either, the general matrix, denoted $[M]$ hereafter, is calculated once for all at the beginning of the simulation and does not change as the simulation progresses. Moreover, $[M]$ is a constant and inversible matrix so it can be inverted once at the initialization of the simulation and stored. The only thing that changes is the right-hand side, denoted $[SM]$ from now onwards. Vector $[SM]$ has to be evaluated at each time increment in order to obtain the set of normal doublet μ_p and the source intensity Q so that the desired velocity field is obtained. This velocity profile is basically a zero normal component on the pipe and is equal to $\boldsymbol{V}_{P_Q^c} = W_{\text{jet}}\boldsymbol{e}_z$ at the centre of the pipe exit section. This last matrix multiplication completes the calculation of velocity $\boldsymbol{U}$. The general form of $\boldsymbol{U}$ is therefore equation (13), $\boldsymbol{U}_\omega$ taking into account the presence of

the particles, $\boldsymbol{U}_s$ for the presence of the point source P_Q^o and $\boldsymbol{U}_\phi$ for the pipe.

$$\boldsymbol{U} = \boldsymbol{U}_\omega + \boldsymbol{U}_s + \boldsymbol{U}_\phi + \boldsymbol{U}_\infty \tag{13}$$

The calculations were performed on a 12-node cluster with Power 4 processors (1.3 GHz, 5.2 GFlops). To give a rough idea of the computation duration, approximately 0.117 s was required for one time step for a thousand particles.

2.3 *Particles emission*

As mentioned above, the Kutta–Joukovsky condition was used to obtain the vorticity that has to be introduced in the emitted vortex blobs. Defining $(\boldsymbol{X}_{bf}, \boldsymbol{t}, \boldsymbol{k}, \boldsymbol{n})$ as a local normalized vector base for each discrete element at the edge of the pipe (see figure 1), the position $\boldsymbol{X}_i$ and the weight $\boldsymbol{\Omega}_i$ of the emitted particle from the ith surface element was obtained as follows:

$$\begin{cases} \boldsymbol{X}_i = \boldsymbol{X}_{bf} + \boldsymbol{U}_{bf}(\delta t/2) & \text{(14a)} \\ \boldsymbol{\Omega}_i = |\boldsymbol{U}_{bf}|\delta t \displaystyle\int_{\delta h_i} \omega_{bf}\, dh & \text{(14b)} \end{cases}$$

where $\boldsymbol{U}_{bf} = (\boldsymbol{U}_{\text{inside}} + \boldsymbol{U}_{\text{outside}})/2$ stands for the mean velocity onto the considered element between the inside and the outside part of the pipe, δh_i represents the width of the discrete element, and $\omega_{bf} = \boldsymbol{n} \wedge (\boldsymbol{U}_{\text{inside}} - \boldsymbol{U}_{\text{outside}})$.

Introducing a vorticity decomposition onto the local vector base ($\boldsymbol{\Omega}_i = \Omega_i^t \boldsymbol{t} + \Omega_i^k \boldsymbol{k}$) and using the fact that the velocity jump is basically the doublet gradient ($\boldsymbol{\nabla}\mu = [\boldsymbol{U}] = (\boldsymbol{U}_{\text{inside}} - \boldsymbol{U}_{\text{outside}})$, the two components of the particle intensity were obtained as follows:

$$\begin{cases} \boldsymbol{\Omega}_i^t = \delta h_i(\mu_i(t+\delta t) - \mu_i(t)) & \text{(15a)} \\ \boldsymbol{\Omega}_i^k = \left|\boldsymbol{U}_{bf}\right| \delta t \dfrac{\mu_{i+1}(t) - \mu_{i-1}(t)}{2} & \text{(15b)} \end{cases}$$

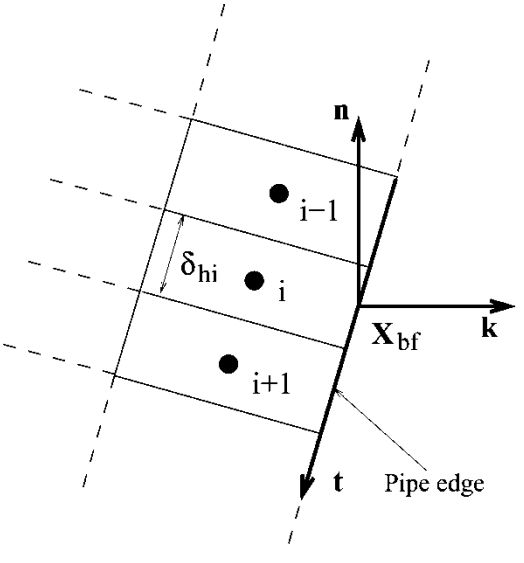

Figure 1. Local normalized vector base definition for the discrete elements at the edge of the pipe.

In the present calculations, an additional iterative procedure was used to enforce the implicit characteristics of the above-described emission scheme.

2.4 *Viscous and turbulent diffusion*

In this section, the discretization of the diffusion term of the Navier–Stokes equation (1b) will be discussed. Chorin's first random vortex method [35], based on random walk, is very efficient for two dimensional (2D) simulation, but seems difficult to apply to 3D cases. Two different methods were subsequently proposed, the PSE (particle strength exchange) method [36, 37] which has a straightforward 3D version, and the diffusion velocity method [38], which was extended to 3D flows in [39]. The first of these methods seems to be the main method used for diffusion in three dimensions and is actually used in this study. The PSE method, as its name points out, models diffusion with a transfer of vorticity from one particle to another without changing the support $\mathcal{P}$ of the blobs. The governing equations that lead to the discrete form are the following. First of all, an expression for the vorticity as in equation (16) is stated.

$$\boldsymbol{\omega}(\boldsymbol{x}) = \int_{\mathcal{V}} \boldsymbol{\omega}(\boldsymbol{x}')\xi_\epsilon(|\boldsymbol{x}-\boldsymbol{x}'|)d\boldsymbol{x}'$$
$$\text{with} \quad \xi_\epsilon(r) = \frac{1}{(\pi\epsilon^2)^{3/2}} exp\left(-\frac{r^2}{\epsilon^2}\right) \tag{16}$$

Starting from this point, the Laplacian of the vorticity field $\triangle\boldsymbol{\omega}$ is defined as in equation (17), defining a function $\eta_\epsilon(r)$ calculated with $\xi_\epsilon(r)$. The expression for the diffusive part of the Navier–Stokes equation (1b) is now obtained by multiplying $\triangle\boldsymbol{\omega}$ with the kinematic viscosity ν.

$$\nu\triangle\boldsymbol{\omega}(\boldsymbol{x}) = 2\nu\int_{\mathcal{V}}(\boldsymbol{\omega}(\boldsymbol{x}')-\boldsymbol{\omega}(\boldsymbol{x}))\eta_\epsilon(|\boldsymbol{x}-\boldsymbol{x}'|)d\boldsymbol{x}'$$
$$\text{with} \quad \eta_\epsilon(r) = -\frac{\nabla\xi_\epsilon.\boldsymbol{r}}{r^2} \tag{17}$$

$\xi_\epsilon(r)$ being a spherical function, $\eta_\epsilon(r)$ can be expressed directly, and the function $\eta_\epsilon(r) = (2/\epsilon^2)\xi_\epsilon(r)$ is obtained. The next step consists of discretizing this last equation (17) and denoting $\mathcal{V}_j$ the volume of the j^{th} particle yields:

$$\nu\triangle\boldsymbol{\Omega}_i \approx \nu(\triangle\boldsymbol{\omega}(\boldsymbol{X}_i))\mathcal{V}_i = 2\nu\sum_{j=1}^{N_\Omega}(\boldsymbol{\Omega}_j\mathcal{V}_i - \boldsymbol{\Omega}_i\mathcal{V}_j)\eta_\epsilon(|\boldsymbol{X}_i-\boldsymbol{X}_j|) \tag{18}$$

This last equation (18) completes the discretization of the diffusive part of the Navier–Stokes equation. A simple turbulent diffusion model is added on top of viscous diffusion. This is an LES model based on enstrophy introduced by Mansour *et al*. [31], defining an eddy viscosity ν_{turb}. The total viscosity ν used in equation (18) is the sum of the viscous term and the turbulent term, $\nu = \nu_{\text{visc}} + \nu_{\text{turb}}$ with:

$$\nu_{\text{turb}} = (C_v h)^2 (2\boldsymbol{\omega}_i\boldsymbol{\omega}_i)^{1/2} \tag{19}$$

A detailed study of a similar LES model was carried out by Mansfield *et al*. [40]. The present simulation used a somewhat simpler version, particularly with respect to the value of the constant C_v, which is fixed a priori and set to a typical value of 0.2. The length h is equal to the smoothing parameter δ, which is an intuitive and widely spread way of determining the sub-grid scale. The motivation for choosing this model is twofold. First it is quite easy to

implement within a particle method. Second, it is built for vorticity diffusion which is exactly what is required.

In this computation, the total viscosity ν was reduced to the eddy viscosity ν_{turb}, since ν_{visc} was assumed to be negligable.

2.5 *Hypothesis of the simulation*

The simulation was run using a round pipe with diameter D equal to 2.0 and length L equal to 5.0. The pipe was discretized into 1800 surface elements with 60 emission points at the pipe exit. The configuration is shown in figure 2 where it can be observed that the coordinates (x, y, z) were defined in order to have the central point of the exit section at the origin $(0, 0, 0)$. Let (u, v, w) be the instantaneous velocity components; the averaging operator $\langle . \rangle$ was introduced so that

$$U = \langle u \rangle = \frac{1}{T} \int_0^T u dt$$

is the mean velocity component in the x-direction. The fluctuation velocity component is then obtained as $\widetilde{u} = u - U$. So (U, V, W) appear to be the mean velocity components and $(\widetilde{u}, \widetilde{v}, \widetilde{w})$ are the fluctuating velocity components for the three directions in space. All distances are measured from the centre of the pipe exit. U_∞ is called the free stream velocity, and W_{jet} the desired velocity at the pipe exit, the angle of injection being fixed at a constant value of 90°. $|V|$ is defined as the euclidian norm of the velocity. The momentum ratio is defined $J = \rho_{\text{jet}} W_{\text{jet}}^2 / \rho_\infty U_\infty^2$ which, for incompressible flows, simplifies to the injection ratio

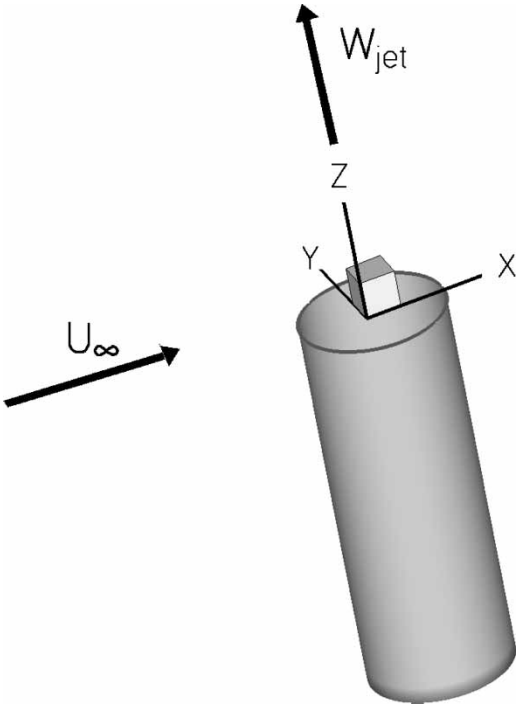

Figure 2. Simulation configuration including the pipe, the coordinates (x, y, z), and the free stream velocity direction U_∞ as well as the jet velocity direction W_{jet}.

$R_{\text{inj}} = W_{\text{jet}}/U_\infty$. As this simulation is by definition incompressible, only the injection ratio R_{inj} is used throughout this paper. The dimensional characteristic L_0 is then chosen as the diameter length $L_0 = D = 2.0$ and the time characteristic T_0 is defined as $T_0 = L_0/U_\infty$, U_∞ being the mean crosswind velocity. The smoothing parameter δ is set to $\delta = 0.15D$.

An important simplification in these calculations is that the effect of buoyancy was completely discounted: this is a non-buoyant jet simulation. According to Kamotani and Greber. [12], it was assumed that this is not a problem because buoyancy only plays a minor role, as jet motion is inertially dominated. Second, this simulation is based on an extended nozzle or a pipe, which differs from the flush-mounted nozzle of most experiments and numerical simulations. As far as is known, only Moussa *et al*. [14] carried out experiments on such configurations with an extended nozzle. However, owing to the simulation configuration, which implies that there is no boundary layer at the nozzle exit, there is no account for the horseshoe vortices which form upstream of the jet. These horseshoe vortices have been studied by Krothapalli *et al*. [25] for rectangular-shaped jets in crossflow and by Andreopoulos [16] for round jets, for instance. It is worth noting that the absence of such vortices may probably influence the flow structure in the near field of the jet.

Concerning the velocity profile at the pipe exit, it is very difficult to have precise and reliable measurements from the experimental studies. In other words, it is very difficult to guess the influence of the crosswind right at the pipe exit or even inside the nozzle, if there is any influence inside. Figure 3 shows the computed axial velocity profile exactly at the pipe exit along the line with the equation being $y/D = z/D = 0.0$. This velocity profile is an ensemble averaged of results over 101 particle fields from dimensionless time $t/T_0 = 25.0$ to $t/T_0 = 27.5$, taken every $\Delta t/T_0 = 0.025$. It is evident that this velocity profile does not look like a top-hat or fully pipe flow profile. So the crosswind does exert an influence on

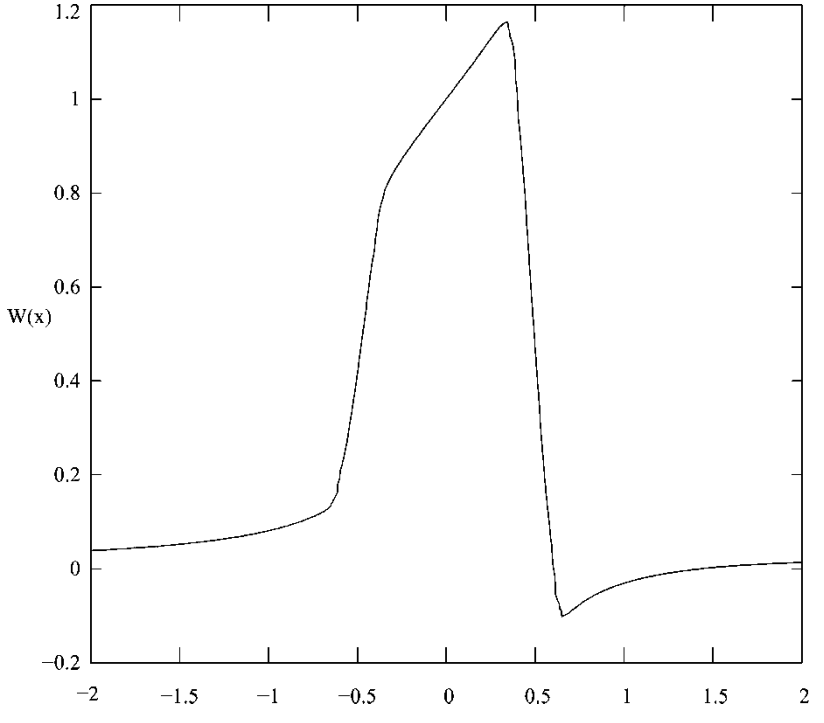

Figure 3. Axial velocity profile right at the pipe exit ($y/D = z/D = 0.0$) for a jet in crossflow ($R_{\text{inj}} = 4.0$). The velocity component $W(x)$ has been averaged over 101 particle fields from dimensionless time $t/T_0 = 25.0$ to $t/T_0 = 27.5$ taken every $\Delta t/T_0 = 0.025$.

the exit velocity profile. In this simulation, the velocity at the nozzle exit was forced to be $W(x = 0, y = 0, z = 0) = W_{\text{jet}} = 1.0$. A careful inspection of this velocity profile shows that $W_{\text{jet}} = 1.0(+/-0.0001)$ right at the center of the exit section. The tubulence intensities have been computed on this profile and the maximum range of velocity fluctuation was in the z-direction equal to $\langle \widetilde{w}^2 \rangle / W_{\text{jet}}^2 = 0.0025$.

Checking the quality of the velocity profile right at the pipe exit is difficult since it was not possible to find any results or measurements with a similar configuration. However, a lot of work has been done on particle simulation of free jets without crossflow, but with a similar value for the smoothing parameter. In these cases, a full pipeflow-like exit velocity profile was obtained. Therefore, it gives some support to this numerical simulation. The effect of the crossflow on the velocity profile at the pipe exit is then of some importance. Some experimental measurements were carried out on round turbulent jets in crossflow for plane z/D located slightly above the exit plane, so only qualitative agreement can be derived. As far as is known, only Kamotani *et al.* [12] measured the velocity profile right at the pipe exit with the presence of the crossflow, and they found it was nearly symmetric. Therefore, the exact shape of the velocity profile at the exit is still unresolved.

3. Raw results and velocity characteristics

3.1 *Numerical and physical parameters*

In this study, several simulations were done with different parameters such as the smoothing parameter, diameter or length of the nozzle, and different nozzle dicretization. An optimal set of parameters was selected in order to obtain the best possible simulation for a reasonable computing time. Several injection ratios have also been used but this paper will only focus on simulations with one injection ratio $R_{\text{inj}} = 4.0$. The reason this injection ratio was chosen is that it belongs to the range of the most commonly used values in the literature ([11] with $R_{\text{inj}} = 4.0, 6.0, 8.0$, [12] with $J = 15.3$ corresponding to $R_{\text{inj}} \sim 4.58$, [13] with $R_{\text{inj}} = 2.37, 3.95, 6.35$, [14] with $R_{\text{inj}} = 3.48$ and finally [27] with $R_{\text{inj}} = 4.6$). As explained earlier, the exit velocity was forced to $W_{\text{jet}} = 1.0$ and the crosswind was then set to $U_\infty = 0.25$ in order to obtain the desired injection ratio. The dimensional characteristics then become $L_0 = 2.0$, $T_0 = L_0/U_\infty = 8.0$, and the dimensionless time increment of the unsteady simulation was $dt/T_0 = 0.025$. The simulation was run over 1500 time increments. Another simulation was run with exactly the same parameters except that regridding was turned off. Results of this simulation will be discussed later on, but it can already be pointed out that they were very close to those with regridding, at least for the beginning of the simulation. Later on they deteriorated rapidly, to finally blow up after 221 time steps. The different characteristics of this simulation are summarized in table 1

Table 1. Summary of simulation characteristics. In the case of (†) the simulation collapsed whereas in the case of (*) the simulation was stopped normally.

Simulation	Without regridding	With regridding
Injection ratio	4.00	4.00
Number of iterations	$221^\dagger$	$1500^\star$
δ/D	0.15	0.15
Maximum number of particles	∼13200	∼83000
Time step: dt/T_0	0.025	0.025

The raw results, i.e. the numerical results made up with particle fields without any post-processing, will be briefly discussed first, and a few observations aparting these fields will be made. Some velocity characteristics of jets in crossflow, including trajectory and self-similar velocity profiles will be presented, as well as a comparison of the computed trajectory with analytical equations based either on theoretical arguments or on experimental data. Then, the vortex dynamic that develops in the near field of the jet will be considered and an attempt will be made to identify the different structures that are listed in other experimental studies, such as vortex rings or the vortex loops. To finish with, the case of the CVP will be discussed.

3.2 *Raw numerical results of a jet in crossflow*

This section deals with raw results of the time-resolved evolution of the jet. This simulation was run with 1500 time increments and the maximum number of particles at the end of the simulation reached more or less 83 000 particles with initially 60 emission points, thus 60 new particles were introduced in the flow at each time step (see table 1). An isometric view and a side view of the locations of the particles is shown in figure 4. For clarity, only one particle out of ten is represented for the bulk of the flow, and one out of three in a restricted volume close to the pipe exit. Data have also been truncated in the x-direction, that is only particles whose positions in the x-abscissa is below $x_{\max} = 25.0$ are shown.

In figure 4, it can be observed that the jet is already developed and that it is well defined in the x-direction, even for x up to 10 diameters. As already mentioned, the particles are not attributed to any particular vortex structure as in Cortelezzi and Karagozian [10] calculations. Therefore, it is quite difficult to identify directly the vortical structures in these views. Although the new particles can be thought of as initially belonging to the same vortex ring, this is no longer preserved by the regridding which has been performed every four steps in this simulation. In spite of this, the regridding is necessary to obtain a good representation of the flow in the far field where the distortions of the original vortex structures become untractable otherwise. Therefore, the regridding procedure was applied and a post-treatment routine was written in

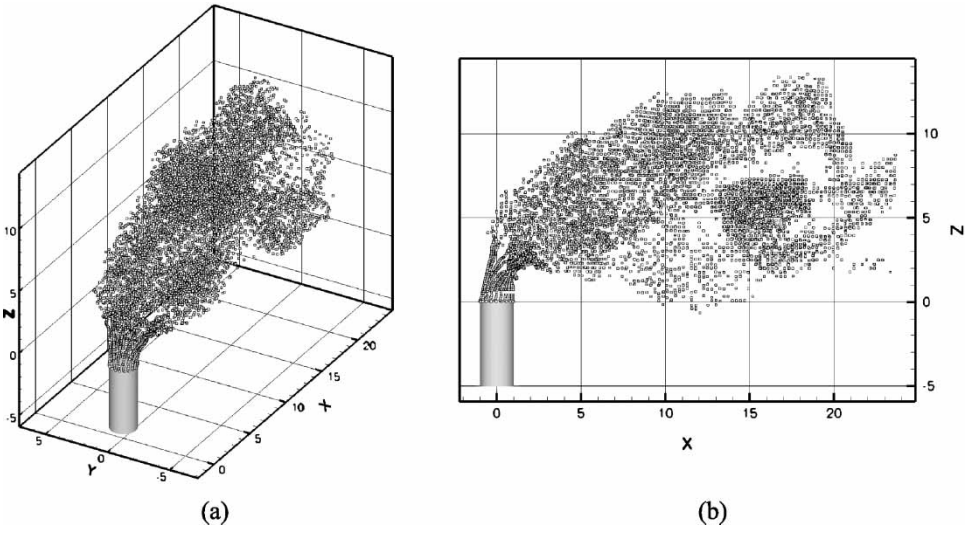

Figure 4. Location of particles at time $t/T_0 = 25.0$ (1000th iteration) for a jet simulation of $R_{\text{inj}} = 4.0$. (a) is an isometric view (b) is a side view. One particle out of three is depicted very near to the pipe exit and one out of ten otherwise. Data have also been truncated in the x-direction for $x \leq 25.0$.

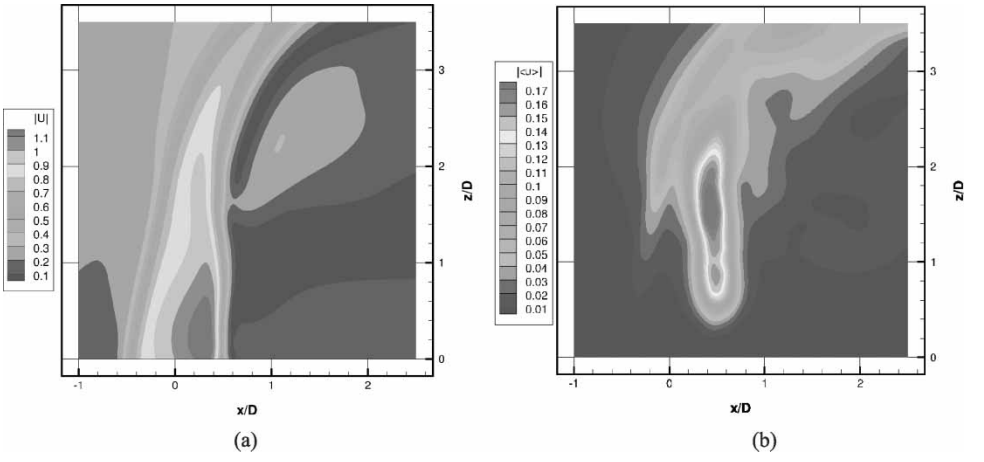

Figure 5. Two dimensional mean velocity (a) and turbulence intensity (b) mapping in the plane of symmetry of the jet simulation, $R_{\text{inj}} = 4.0$. The averaging has been performed over 101 particle fields from dimensionless time $t/T_0 = 25.0$ to $t/T_0 = 27.5$.

order to achieve the identification of the vortical structure. The velocity and vorticity field on a 3D cartesian grid were extracted from the numerical simulation together with some invariants of the flow field.

3.3 *Two-dimensional velocity and turbulence intensity mapping*

An averaging procedure was used to obtain a 2D mean velocity mapping in the symmetry plane of the jet for time ranging from $t = 25.0T_0$ to $t = 27.5T_0$. The iso-value of the velocity norm $|V|$ is shown in figure 5(a) where the usual potential core is visible as a region where the value of $|V|$ is conserved as it was at the exit. The asymmetry of the potential core owing to the crossflow is also visible. It may be related to the asymmetry of the velocity profile at the nozzle's exit [figure 3]. This deflection of the potential core has experimentally been observed by Keffer and Baines [11] for the same injection ratio $R_{\text{inj}} = 4.0$. They attributed this phenomenon to the strong pressure field around, and consequently within, the jet. As a result, the potential core also differs from that of a free jet in that the maximum velocity is above the prescribed velocity $W_{\text{jet}} = 1.0$ at the nozzle's exit. The maximum velocity recorded in these calculations is $|V| = 1.18$.

The 2D mapping of turbulence intensity corresponding to the case of figure 5(a) is shown in figure 5(b). The computed quantity $|\langle u \rangle|$ is the euclidian norm of the dimensionless normal turbulence intensities defined as:

$$|\langle u \rangle| = \sqrt{\frac{\langle \widetilde{u}^2 \rangle + \langle \widetilde{v}^2 \rangle + \langle \widetilde{w}^2 \rangle}{W_{\text{jet}}^2}}$$

It can be observed that the maximum turbulence intensity is around 17%. The turbulent intensity field exhibits a strong asymmetry, as in the case for mean velocity. It is almost impossible to detect the vorticity shear layer developing in the upstream part of the jet with the levels defined here in the legend, whereas the lee-side of the jet seems to be the locus of an intense turbulent phenomenon. This tremendous difference between the upstream and downstream behaviour of the jet is rather surprising. In the following sections an attempt is made to identify the reasons of such disparity between the two sides.

3.4 *Jet trajectory*

This section deals with the calculation of jet trajectories. There are different approaches to the calculation of these trajectories. Some are based on velocity maxima as in Chassaing *et al*. [13] and Kamotani *et al*. [12] for the experimental side, and Yuan and Street [8] for the numerical one. Other authors such as Humber *et al*. [26] used the concentration of a passive scalar for a rectangular jet in crossflow or temperature maxima, as Kamotani and Greber [12], to define the jet trajectory.

In the present study, jet trajectories were calculated as the loci of maximum velocities along a defined cross-section. This is the most common measure of jet trajectory used in experiments. The *modus operandi* is the following: first, a cross-section is defined which crosses the pipe centre ($x = y = z = 0.0$), parallel to the x-direction (the direction of the cross stream in the study). A computational grid profile is then built in this section and the ensemble-average velocity is evaluated on the grid points. The point having the maximum velocity modulus is then selected as the first point of the jet trajectory. A new cross-section profile is defined in the plane perpendicular to the velocity at this maximum velocity point at a distance equal to $ds = 0.02 * D$, and the procedure is repeated iteratively. This is a step-by-step construction of the jet trajectory. The ensemble-average velocity is evaluated based on 41 particle fields from dimensionless time $t/T_0 = 17.5$ to $t/T_0 = 27.5$ with a $dt/T_0 = 0.25$.

Figure 6 shows the computed trajectory obtained by application of the above-described procedure, compared with trajectories obtained with the same maximum velocity criterion by other authors. It can be observed that the agreement is quite good with the experimental equations of Chassaing *et al*. [13] and Kamotani and Greber [12], the Shandorov empirical model given in [41] as well as with the theoretical equation of Ivanov also taken from [41]. The general form of these fitted equations is

$$(z/D) = (a * R_{\text{inj}}^{b} + c) * (x/D)^{d} \tag{20}$$

The L_2 normalized error between calculations from this study, and an average of the published results remains close to $\text{err}_{L_2} \sim 0.1$ for the injection ratio $R_{\text{inj}} = 4.0$. Beside this, the maximum error for the results used for the comparison is 14%, the maximum

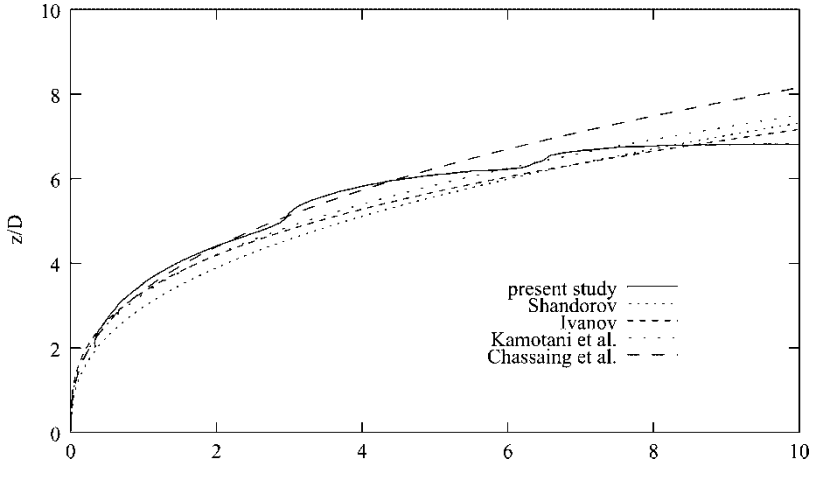

Figure 6. Maximum velocity-based trajectory of a jet in a crossflow for $R_{\text{inj}} = 4.0$. The ensemble-average velocity is evaluated based on 41 particle fields from dimensionless time $t/T_0 = 17.5$ to $t/T_0 = 27.5$ with a $dt/T_0 = 0.25$.

being observed for Shandorov and Chassaing [13]. One possible explanation for this error is the absence of any account for Reynolds numbers with injection ratio effect in equation (20).

The trajectory identification starts at $z/D = 2.0$ owing to the fact that the velocity is supposed to be rather homogeneous and satisfying $|V| \sim W_{\text{jet}}$ in the potential core, right at the pipe exit. Therefore, the trajectory algorithm experiences troubles in detecting a maximum. This in turn leads to meaningless results which are not actually reproducible. Moreover, this error on the first computed point of the jet trajectory yields a trajectory always lying slightly downstream of equation (20). This is quite obvious due to the deflection of the potential core which is far from being symmetric (see section 3.2). The power law fits are not able to account for this disymmetrization of the potential core as their starting point was arbitrarily set right in the middle of the exit section ($x/D = y/D = z/D = 0.0$). Moreover, as far as is known, it is very difficult to secure accurate measurements in the near field at the pipe exit. Almost all the measurements of Kamotani and Greber [12] as well as those of Chassaing *et al*. [13] have been done above the plane $z/D = 1.0$.

3.5 *Self-similarity & velocity profiles*

As in free jets, a jet to crossflow can be divided into three main parts. First, a potential core where the velocity is mainly constant and the flow is potential. In the case of a jet in crossflow, this potential core is noticeably smaller than the one for a free jet, owing to the expansion of the shear payers by the cross-stream, as shown in figure 5(a). Then, a transitional zone where the flow can no longer be considered as potential and where the mixing of the flow becomes more and more significant, and finally the main zone that corresponds to the zone of establishment of the velocity profile self-similarity. For free jets, the self-similar velocity profiles are obtained by rescaling the velocity profile in a cross-section, using the maximum velocity and the jet diameter as velocity and length scales, respectively. The same procedure applies to crossflow jets as observed in figure 7. The same method of rescaling was used as the one of Chassaing *et al*. [13], which leads to an equation of the kind:

$$|V|_{\parallel}/|V|_{\max} = f(\eta), \quad \eta = r/r_{\lambda} \tag{21}$$

where f is a function to be determined and most frequently identified as the Tollmien's law. In the previous equation (21), $|V|_{\max}$ is the maximum velocity modulus on a considered

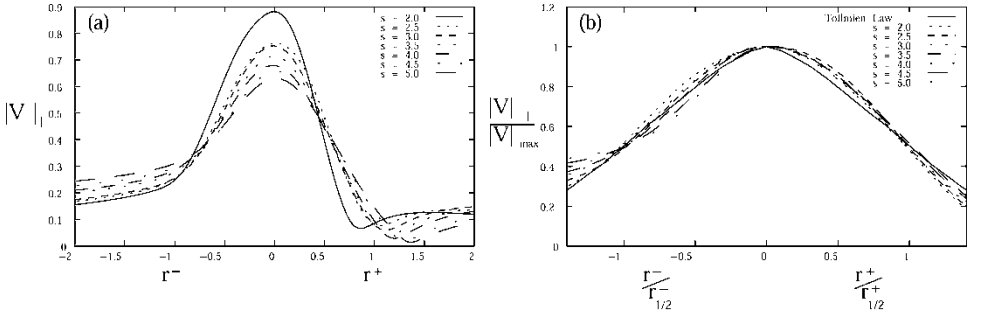

Figure 7. Axial velocity profiles for the jet in crossflow, $R_{\text{inj}} = 4, 0$. (a) represents the axial velocity profiles transferred on the r-abscissa and (b) represents the similarity law for the dimensionalized velocity profiles after Chassaing *et al*. [13]. The ensemble-average velocity has been computed over 41 particle fields from dimensionless time $t/T_0 = 17.5$ to $t/T_0 = 27.5$ with a $dt/T_0 = 0.25$.

profile, $|V|_{\parallel}$ is the local velocity component parallel to the direction of $|V|_{\max}$ and r is the algebraic distance between the point considered and the grid point of the maximum velocity modulus. Finally, r_λ is defined as the following $|V|_{\parallel}(r_\lambda) = \lambda * |V|_{\max}$, and for λ a common value of $\lambda = 0.5$ was chosen. Results of figure 7(b) show that the rescaled velocity profiles are very close to the Tollmien's law, and figure 7(a) the associated crude velocity profiles.

4. Elements on the vortex dynamic of a jet in crossflow

4.1 *Vortex identification*

The azimuthal component ω_y is by far the most dominant component of the vorticity field in the symmetry plane of the jet, as can be observed by comparing figure 8(a) and 8(b). A

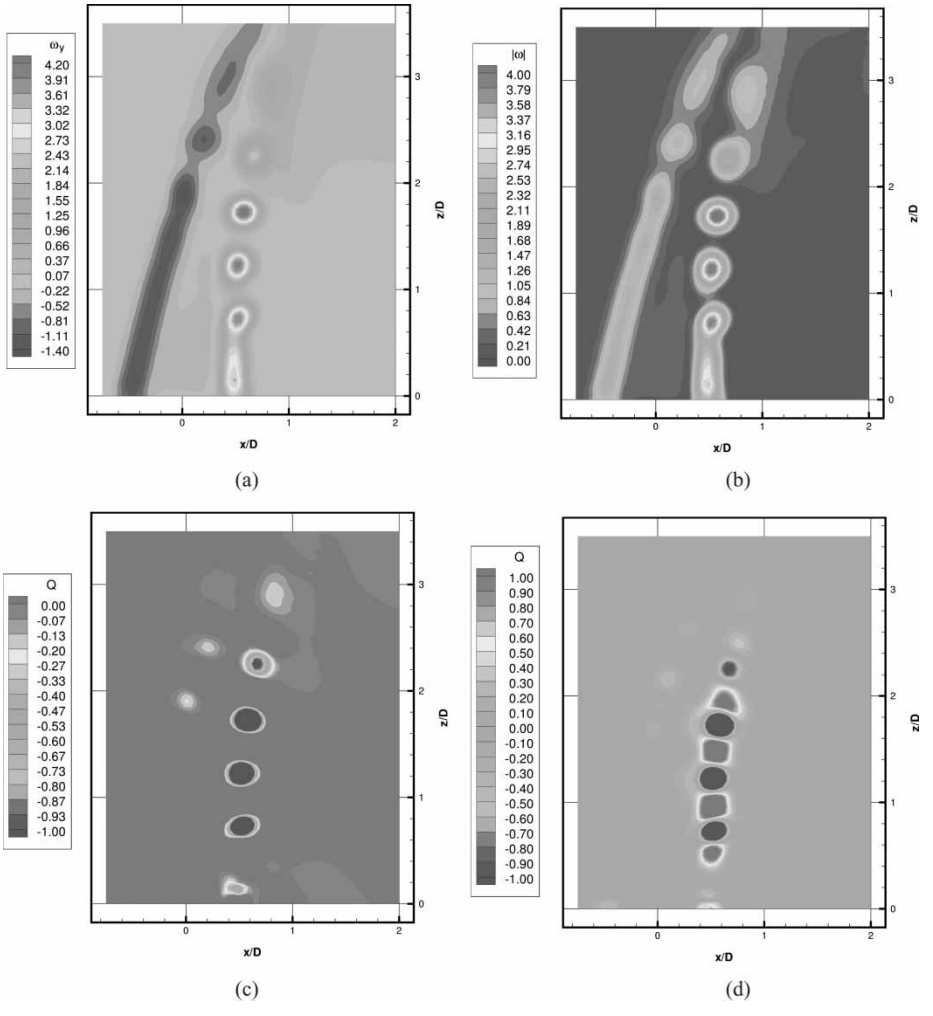

Figure 8. Identification of vortical structures for a jet in a crossflow ($R_{\text{inj}} = 4.0$) in the symmetry plane for an instantaneous flow configuration at time $t/T_0 = 18.0$ (720th time step). (a) vorticity modulus contour, (b) ω_y contour, (c) and (d) Q with two different scales.

noticeable difference between the downstream and upstream layers is the onset of vorticity patches on the former, whereas a quasi-uniform vorticity layer is observed upstream. This is obviously the trace of a rolling-up occuring downstream, potentially yielding the vortex ring also observed by Kelso *et al.* [18]. At this stage, from this study it cannot be stated whether these structures are actual vortex rings or not because a large part of these rings merge within the upstream vortex layer.

There are many factors contributing to the different behaviour between the upstream and downstream shear layer. First, the curvature is higher downstream, second the vorticity is lower upstream due to the asymmetry of the velocity profile at the pipe exit, and third the stretching induced by the free stream is higher upstream.

Vorticity is one possible candidate to detect coherent vortical structures, as is strain. However, an alternative preferred by some authors [23, 42] is to use the second invariant of the velocity gradient tensor, denoted Q hereafter, as a more informative flow identifier. In the study case of incompressible flow, Q is the following

$$Q = -\frac{1}{2}u_{i,j}u_{j,i} = \frac{1}{2}(tr[AA^t] - tr[SS^t]) \quad \text{and} \quad u_{i,j} = \frac{\partial u_i}{\partial x_j} \tag{22}$$

where S and A are respectively the symmetric and anti-symmetric part of the velocity gradient tensor. Therefore, this quantity will be negative in the region of strong vorticity and positive in the region of strong stretching. This indicator is expected to be better able to detect vortex cores than vorticity.

Maps of Q with two different colour scales are also shown in figure 8(c) and 8(d). Well-defined vortices can be observed downstream, whereas the upstream layer is hardly detectable. Only a few weak vorticity patches appear at the top of the figure, indicating that a less active rolling-up process has started there. These views are rather similar to pictures obtained by Ganaputhisubramani *et al.* [23] for the round jet case. The last observation concerns the inter-distance between two associated vortices. It is clearly decreasing as they are convected downstream. This provides an argument supporting the assumption by Kelso *et al.* [18] of the existence of folded and tilted vortex rings.

4.2 *Generation of the primary vortex ring*

This section is devoted to the primary vortex ring formation at the pipe exit. The dynamics of jet-associated vortex rings has been extensively studied by Kelso *et al.* [18], who have hypothesized that vortex rings are generated right at the top of the nozzle's exit thanks to the shear layer roll-up. After the ring completion, it starts to convect and, at the same time, starts to tilt and fold.

The vortex ring generation can be observed from Q iso-surfaces. Figures 9(a) to (f) display different times for both isometric and side view. Figures 9(a) and 9(b) represent vortex structures at different dimensionless times ranging from 0.5 to 1.0. The first vortex ring, generated by the rolling-up of the vortex shear layer, can be observed clearly. This vortex ring is not axisymmetrical owing to the asymmetry of the upstream and downstream rolling-up activity already mentioned. The matching between the upstream shear layer and the vortex rings cannot be observed owing to the fact that Q only tracks vortices and ignore shear layers. At $t/T_0 = 0.75$, in figure 9(d), the folding of the vortex ring has already started, presumably owing to the crosswind influence as assumed by Kelso *et al.* [18]. This folding is even more obvious in figure 9(f) for $t/T_0 = 1.0$. However, at the later time, the Q isovalue evolves in forming an open ring for later times, indicating a consequent modification in the rolling-up process downstream.

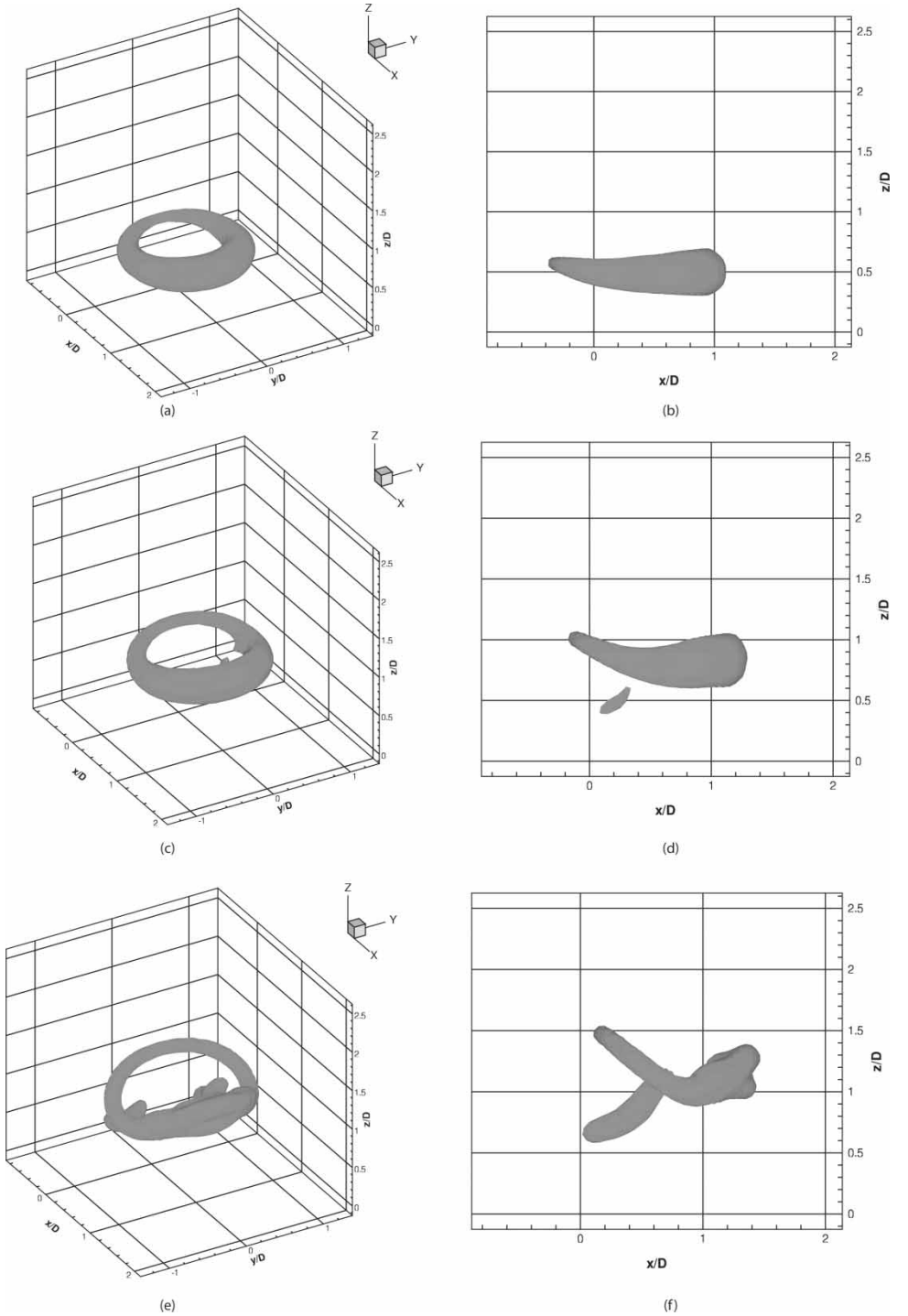

Figure 9. Iso-surface of $Q = -1.0$ for a jet in crossflow with an injection ratio $R_{\text{inj}} = 4.00$. (a), (c) and (e) give isometric views, (b), (d), and (f) give side views. (a) and (b) correspond to $t/T_0 = 0.5$ (20th time step), (c) and (d) correspond to $t/T_0 = 0.75$ (30th time step), (e) and (f) correspond to $t/T_0 = 1.0$ (40th time step).

In the meantime, two small patches appear slightly under the main vortex ring. They are roughly orthogonal to the folded part of the ring, and develop rapidly to form a structure which can be identified on later views as the premiss of the CVP. This point will be the topic of section 4.4.

4.3 *Vortex rings dynamic at the pipe exit*

Figure 10 shows the evolution of the vortical structures of the jet in crossflow at different times. The simulation was run over 1500 time increments with a quasi-constant number of 83 000 particles at the end of the simulation. By then a steady state was almost reached, with a linear impulse slightly oscillating around mean values.

Compared with the well-defined vortex ring of figure 9, a somewhat different picture is now observed. The opening of the vortex ring in figure 10(a) become wider and wider up to the point where only a reduced vortex tube portion is detectable downstream. However, this remaining part is sufficiently persistent to allow for the observation of three consecutive structures, suggesting that a periodic regime has been reached. The orthogonal vortex structures which have been detected previously are now well developed with a quasi-steady location [figure 10(e) and 10(f)].

There is doubt regarding the true nature of these vortex structures. In a recent paper, Lim *et al*. [27] concluded that there is no evidence that there are actual vortex rings within the flow. They suggested that the CVP is not directly the result of the tilting and folding mechanism identified by Kelso *et al.* [18] and Cortelezzi *et al.* [10], but that of the rolling-up of the cylindrical vortex shear layer under the crossflow influence, eventually yielding some kind of CVP-like vortices. It can be pointed out that this study partially supports this assumption. With the possible exception of the earlier stage of the flow, the CVP is generated independently of the vortex loops.

Figure 11(a) shows iso-surface of vorticity modulus for $|\omega| = 2.0$, and figure 11(b) shows contours of vorticity modulus in the symmetry plane of the jet. Using the Lim *et al*. nomenclature [27], both upstream and lee-side vortex loops can be identified, denoted respectively A and B on figures 11(a) and (c). On figure 11(b), it can observed that the vorticity of the upstream loops is actually weaker than that of the lee-side vortices. This difference is enhanced on figure 11(d), where the vortex identifier Q has been used.

Looking at the details of figure 11(d), three strong lee-side vortex loops are observed, with two more at a weaker level. Three upstream vortex loops are also present. The Q patch right at the pipe exit on the lee-side must not be considered as an additional vortex loop, and is no more than a boundary artefact. It seems that the three upstream vortex loops are associated with the three corresponding lee-side ones. The distance between them becomes smaller as they rise in the z-direction. It seems that the counterpart upstream vortex of the fourth lee-side vortex loop has not yet been created or, in other words, that the shear layer has not started to roll up as shown in figure 11(b). One can certainly conclude that these upstream and lee-side vortex loops are working in pairs. Considering the low level patch denoted C in figure 11(d), it looks like a lee-side vortex loop vanishing owing to a turbulent process as suggested by Lim *et al*. [27]. The associated upstream vortex loop has already disappeared, either owing to the same turbulent process or owing to a merging with the lee-side vortex. Unfortunately, it was not possible to determine which one of these two mechanisms was actually working from the present calculations.

In summary, two main different behaviours were identified from these simulations in the unsteady dynamic of the jet. First, at the very beginning, an initial vortex ring is created,

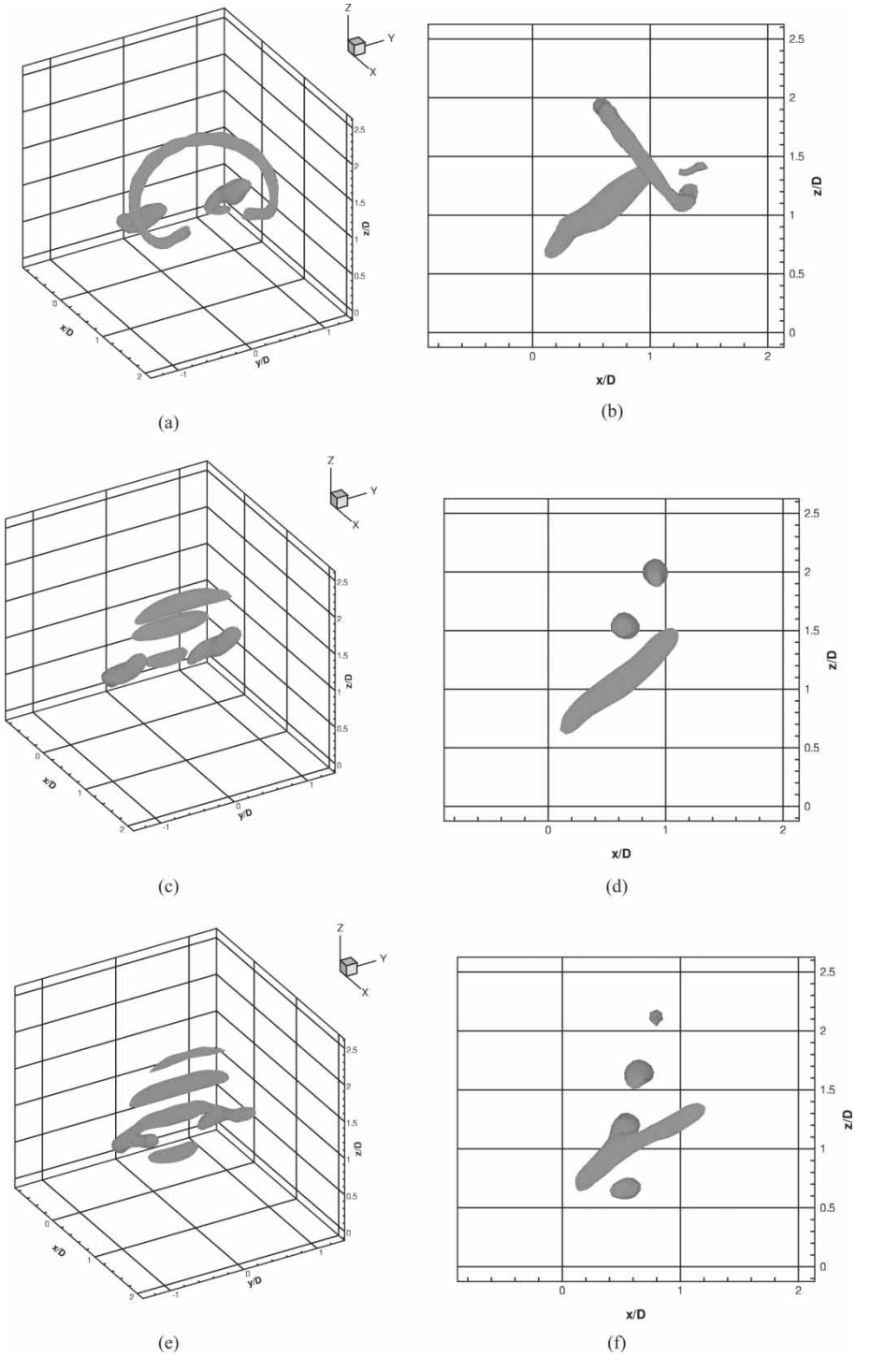

Figure 10. Iso-surface of $Q = -1.0$ for a jet in crossflow with an injection ratio $R_{\text{inj}} = 4.00$. (a), (c), (e): isometric view; (b), (d), (f): side view. (a) and (b) correspond to $t/T_0 = 1.25$ (50th time step), (c) and (d) to $t/T_0 = 2.5$ (100th time step) and (e) and (f) to $t/T_0 = 5.0$ (200th time step).

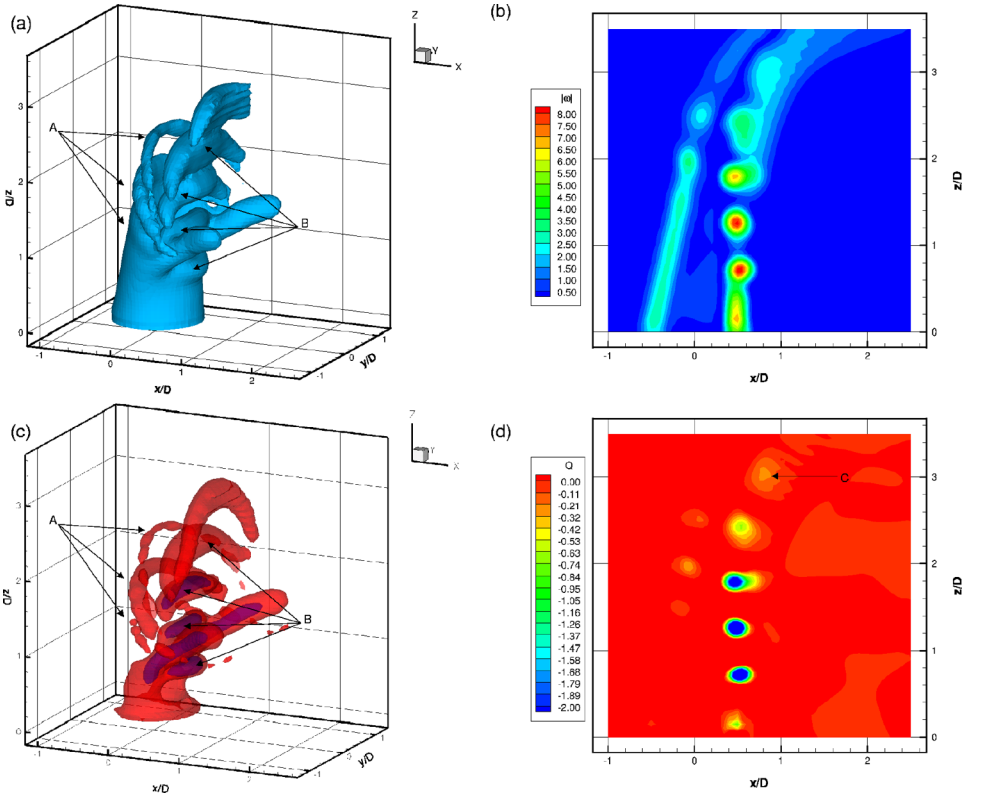

Figure 11. Instantaneous vortical structures at time $t/T_0 = 25.0$ (1000th time step) for a jet in crossflow ($R_{inj} = 4.0$). (a) and (c) give 3D angular views; (b) and (d) give cross-sections of the jet in the symmetry plane. (a) depicts iso-surface modulus of vorticity $|\omega| = 2.0$ and (b) modulus of the vorticity contours. (c) Depicts two iso-surfaces of Q modulus (blue for $Q = -0.9$ and red for $Q = -0.1$) and (d) shows contours of Q restricted to its negative values.

whose shape depends essentially on the initial velocity profile (see figures 9(a) to 9(d)). Then a transition phase appears, as described in figures 9(e) and 9(f), with the folding of this vortex ring and later on with the opening of the ring itself, as in figures 10(a) and (b). Finally a new structure appears, similar to those of figures 10(c) and (d). This new structure first appears approximately at the 100th time increment, and then is almost periodic with good reproducibility [refer figure 11(a) to (d)].

A last interesting feature of these plots is the presence of the CVP, which has been excluded from the earlier partial conclusion. The CVP can clearly be identified on both figures 11(a) and (c) and will be further discussed in the next section.

4.4 *The counter-rotating vortex pair*

This phenomenon has been examined extensively by Cortelezzi and Karagozian [10] in their simulations. By superimposing the 3D iso-surface of the averaged vorticity field to the locations of the particles they concluded that the onset of the CVP is the result of the vortex rings folding. As already mentioned, Lim *et al*. [27], on the contrary, considered that the CVP is initiated by folding of the cylindrical shear layer [see figure 12(a)]. In order to investigate the respective validity of these two scenarios, projections of the particles' location contained within a thin

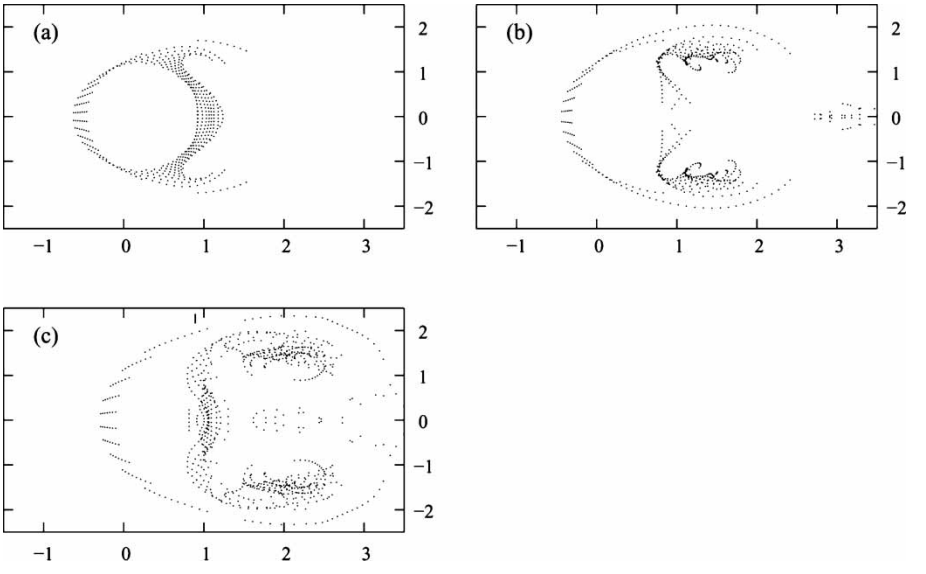

Figure 12. Projection on a x–y plane of the particles located in a slice. Simulation with an injection ratio $R_{\text{inj}} = 4.00$ with no remeshing, time $t/T_0 = 2.75$ (110th iteration): (a) $z \in [1.5 - 2.1]$, (b) $z \in [2.1 - 2.7]$, (c) $z \in [2.7 - 3.3]$.

slice surrounding four selected cross-sections are provided in figure 12. The observed vortex structures are very similar to those described by Lim *et al*. Although in qualitative agreement with the experiments of Lim *et al*., these calculations are not believed to provide any definitive argument in favour of their analysis.

Beside this, several reasons can be given in favour of vortex ring folding as the mechanism responsible for the onset of the CVP. First, folding appears at a point which is confounded with the origin of the CVP patches. This argument is further supported by figures 13(a) and (b), where it can be seen that vortex patches are actually connected to the primary vortex ring by vortex filaments. Therefore, the interpretation of the whole structure as one single vortex ring or independently developing structures is a matter of point of view and flow representation rather than strong evidence. The highly stretched vortex filaments at the attachment point can undergo very different dynamic from the action of each part of the ring. A second argument

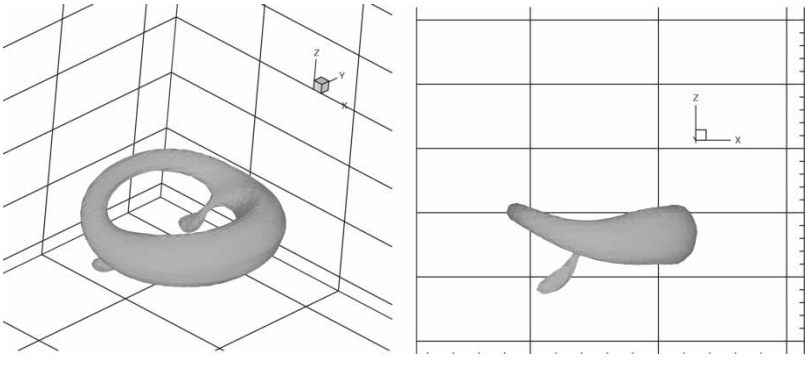

Figure 13. Iso-surface of $Q = -0.9$ for a jet in crossflow ($R_{\text{inj}} = 4.0$) for dimensionless time $t/T_0 = 0.75$ (30th iteration). (a) is angular view and (b) is side view.

must be considered in support of this interpretation: the mechanism suggested by Lim *et al*. as the primary cause for the rolling-up of the cylindrical shear layer is the interaction with the crosswind. This interaction with the crosswind would be able to induce tilting and folding of the vortex rings as well.

This idea would lead to the conclusion that the presence of vortex rings or upstream and lee-side vortices, probably with 'side arms', are not antinomic but may be coexistant, or consecutive phenomena of the vortex dynamic of a jet in crossflow. The location of the transition zone, if there is any, from one structure to the other is not clearly identified yet and may vary owing to the injection ratio, the viscosity of the fluid, or the initial configuration.

Although the origin of the CVP will probably remain controversial, it is generally believed that this structure is very strong and self-supported. To point out this self-supporting property, one can look at the part of the momentum flux from the cross-stream that is dedicated to the feeding of the CVP. Figure 14 shows streamlines starting upstream of the jet nozzle in the far field, going round the main stream of the jet, and rolling up around the Q iso-surfaces defining one arm of the CVP. Owing to its ability to pick up energy from the crossflow, the CVP will grow up to a critical state, at which stage it constitutes a relatively steady structure within the unsteady flow. Lastly, the CVP is a very active mixer as illustrated by figure 15. Streamlines issuing from a relatively concentrated zone in the upstream side of the jet become completely dispersed after having rolled-up around one arm of the CVP.

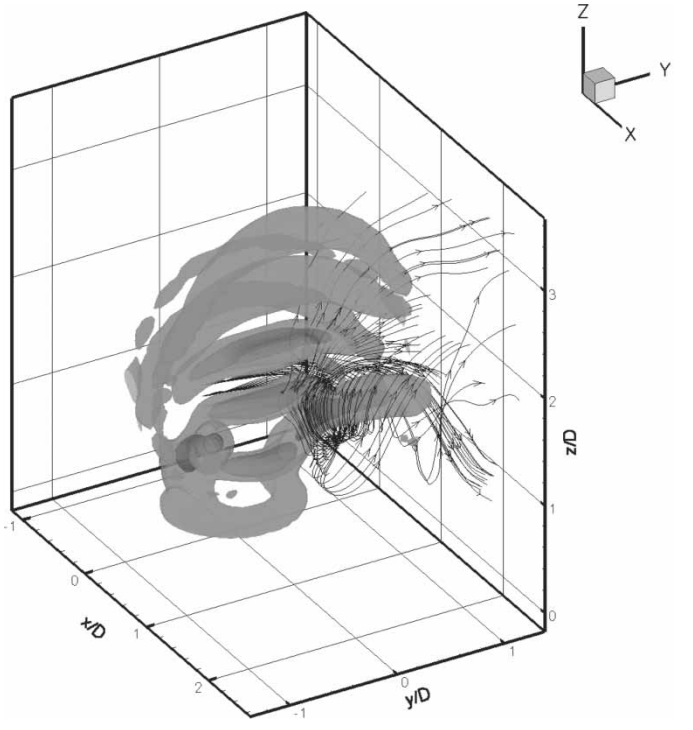

Figure 14. Isometric view of the CVP: iso-surfaces $Q = -1.0$ (blue) and $Q = -0.1$ (green) for a jet in cross-flow with an injection ratio of ($R_{\text{inj}} = 4.0$). Instantaneous field at dimensionless time $t/T_0 = 25.0$ (1000th time step). Streamlines are added in order to spotlight the effect of mixing and feeding of the CVP by the the cross-stream momentum flux.

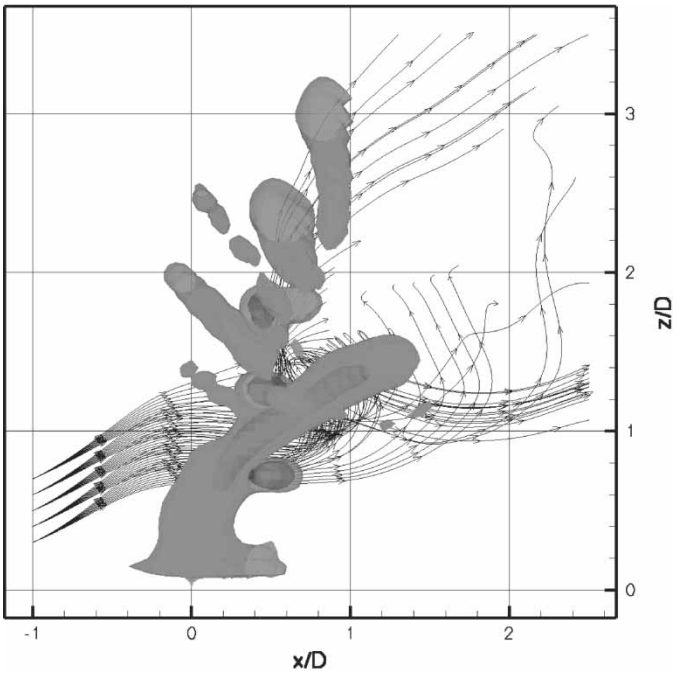

Figure 15. Side view of the CVP: iso-surfaces $Q = -1.0$ (blue) and $Q = -0.1$ (green) for a jet in cross-flow with an injection ratio of ($R_{\text{inj}} = 4.0$). Instantaneous field at dimensionless time $t/T_0 = 25.0$ (1000th time step). Streamlines are added in order to spotlight the effect of mixing and feeding of the CVP by the the cross-stream momentum flux.

5. Concluding remarks

Numerical simulations of a jet in crossflow by means of a vortex particle method were presented for a single injection ratio equal to $R_{\text{inj}} = 4.0$. Owing to the use of a regridding procedure, it was possible to obtain results in the near field as well as in the far field. The longest calculation was run over 1500 time increments, starting from the initial state with no jet up to an almost steady mean flow. Different states of the jet evolution were identified. In particular, the stage running from the first 200 time increments was investigated. One focus area was the onset of the different vortex structures, although no horseshoe vortex was present in the simulation owing to its particular geometrical configuration. Besides this, an interesting feature of the simulation was the possibility of having the velocity profile at the pipe exit establishing itself rather than being prescribed. As a result, this is a non-symmetric profile and it seems that this is of great importance for the jet's early development stages. In future work, quantification of this effect would require a better control of the flow at the exit. Nevertheless, this study highlights the fact that a primary vortex ring appears in the simulation, a phenomenon which probably would have been intensified with a more symmetric exit velocity profile. Additionally, as the jet evolves, this primary ring disappears, allowing the set-up of a more complex structure, similar to that described by Lim *et al*. [27]. In fact, the so-called upstream and lee-side vortex loops could clearly be identified. Side arms, which were expected to connect these structures, were not properly observed, possibly because of an insufficient discretization, although vortex filaments are obviously closed lines in the simulation.

As regards the velocity characteristics, an asymmetric potential core was also observed. This is a common feature of jets in crossflow, and a similar deflection of the potential core was

already pointed out for a similar set of parameters by Keffer and Baines [11]. The asymmetry noticed on the turbulent intensity $|\langle u \rangle|$ can be attributed to some extent to the above described vortex structure dynamic. The jet central line was also computed using a procedure based on velocity maxima. Although this is somewhat arbitrary, owing to the difference in the experimental set-up, results show good agreement with former theoretical and experimental results. The consistancy of the present calculation was further demonstrated by the self-similarity of the velocity profiles computed according to Chassaing *et al*. [13].

The onset of the CVPs was also investigated. The location of the region where they first appear is in good agreement with previous observations by Cortelezzi and Karagozian [10]. Although the process underlying the CVP onset could probably be attributed to different phenomena, by Kelso *et al*. [18] and Lim *et al*. [27], it was not possible to conclude this with an absolute certainty. A further investigation of this crucial point is planned for the future.

Acknowledgements

Gregory Pinon and Hervé Bratec were supported by a grant from Région Haute-Normandie and Hurel-Hispano, a SNECMA group company. The authors would also like to thank Hurel-Hispano for its special support concerning Geoffroy Pignot. Finally, the authors greatfully acknowledge computer time provided by the CRIHAN (Centre de Ressource Informatique de HAute-Normandie).

None of us ever met Professor J. H. Ferziger. However, his name was quite familiar to us as it must probably be to everybody who wants to compute turbulent, or at least vortical, flows. For the older ones among, he was one of the very first to carry out convincing LES simulations and S. Huberson still remembers how he and his colleague at ONERA were following his more recent papers in the 1980s. To E. Rivoalen, he was one of the key references when he started to work on turbulence in the 1990s. We believe that LES is the right method to produce turbulent flow with particles methods and a lot of essential physical aspects trace back to J. H. Ferziger's pioneering work. When we started with this simulation at the dawn of the 21st century, G. Pinon was provided with a lot of papers we had 'on stock' and he had to select those which will be the more helpful among this abundant literature. It is not a surprise that two papers by J. H. Ferziger, [31] and [7], were in that selection. We really believe that the work of J. H. Ferziger will always constitute a reference for much of the next scientific generation, and we would like to take this opportunity to address to him a great gratitude for his helpful contributions.

References

[1] Boersma, B.J., Brethouwer, G. and Nieuwstadt, F.T.M., 1998, A numerical investigation on the effect of the inflow conditions on the self-similar region of a round jet. *Physics of Fluids*, **10**, 899–909.
[2] Grinstein, F.F. and Devore, C.R., 1996, Dynamics of coherent structures and transition to turbulence in free square jets. *Physics of Fluids*, **8**, 1237–1251.
[3] Grinstein, F.F., 2001, Vortex dynamics and entrainment in rectangular free jets. *Journal of Fluid Mechanics*, **437**, 69–101.
[4] Bogey, C. and Bailly, C., 2002, Downstream subsonic jet noise: link with vortical structures intruding into the jet core. *Comptes Rendus Mecanique, Academic Sciences*, Paris **330**, (8 IIb), 527–533.
[5] Bogey, C., Bailly, C. and Juve, D., 2003, Noise investigation of a high subsonic, moderate Reynolds number jet using a compressible LES. *Theoretical and Computational Fluid Dynamics*, **16**, (4) 463–471.
[6] Rembold, B., Adams, N.A. and Kleiser, L., 2002, Direct numerical simulation of a transitional rectangular jet. *International of Journal Heat and Fluid Flow*, **23**, 547–553.
[7] Yuan, L.L., Street, R.L. and Ferziger, J.H., 1999, Large-eddy simulations of a round jet in crossflow. *Journal of Fluid Mechanics*, **379**, 71–104.
[8] Yuan L.L. and Street, R.L., 1998, Trajectory and entrinment of a round jet in crossflow. *Physics of Fluids*, **10**, (009) 2323–2335.

[9] Priere, C., Gicquel, L.Y.M., Kaufmann, P., Krebs, W. and Poinsot, T., 2004, Large eddy simulation predictions of mixing enhancement for jets in cross-flows. *Journal of Turbulence*, **5**, (005).

[10] Cortelezzi, L. and Karagozian, A.R., 2001, On the formation of the counter-rotating vortex pair in transverse jets. *Journal of Fluid Mechanics*, **446**, 347–373.

[11] Keffer, J.F. and Baines, W.D., 1963, The round turbulent jet in a cross-wind. *Journal of Fluid Mechanics*, **15**, 481–496.

[12] Kamotani, Y. and Greber, I., 1972, Experiments on a turbulent jet in a cross flow. *AIAA Journal*, **24**, 1425–1429.

[13] Chassaing, P., George, J., Claria, A. and Sananes, F., 1974, Physical characteristics of subsonic jets in a cross-stream. *Journal of Fluid Mechanics*, **62**, 41–64.

[14] Moussa, Z.M., Trischka, J.W. and Eskinazi, S., 1977, The near field in the mixing of a round jet with a cross-stream. *Journal of Fluid Mechanics*, **80**, 49–80.

[15] Crabb, D., Durao, D.F.G. and Whitelaw, J.H., 1981, A round jet normal to a crossflow. *ASME Journal of Fluids Engineering*, **103**, 142–153.

[16] Andreopoulos, J., 1985, On the structure of jets in crossflow. *Journal of Fluid Mechanics*, **157**, 163–197.

[17] Fric, T.F. and Roshko, A., 1994, Vortical structure in the wake of a transverse jet. *Journal of Fluid Mechanics*, **279**, 1–47.

[18] Kelso, T.T., Lim, R.M. and Perry, A.E., 1996, An experimental study of round jets in cross-flow. *Journal of Fluid Mechanics*, **306**, 111–144.

[19] Panchapakesan N.R. and Lumley, J.L. 1993, Turbulence measurements in axisymmetric jets of air and helium. 1 air jet. *Journal of Fluid Mechanics*, **246**, 1997–223.

[20] Hussein, H.J., Capp, S.P. and Georges, W.K., 1994, Velocity measurements in a high-Reynolds-number, momentum-conservuing, axisymmetric turbulent jet. *Journal of Fluid Mechanics*, **258**, 31–75.

[21] Warda, H.A., Kassab, S.Z., Elshorbagy, K.A. and Elsaadawy, E.A., 1999, An experimental investigation of the near-field region of free turbulent round central and annular jets. *Flow Measurement and Instrumentation*, **10**, 1–14.

[22] Xu, G. and Antonia, R.A., 2002, Effect of different initial conditions on a turbulent round free jet. *Exps in Fluids*, **33**, 677–683.

[23] Ganapathisubramani, B., Longmire, E.K. and Marusic, I., 2002, Investigation of three dimensionality in the near field of a round jet using stereo PIV. *Journal of Turbulence*, **3**, (016).

[24] Krothapalli, A., Baganoff, D. and Karalchetti, K., 1981, On the mixing of rectangular jets. *Journal of Fluid Mechanics*, **101**, 201–220.

[25] Krothapalli, A., Lourenco, L. and Buchlin, J.M., 1990, Separated flow upstream of a jet in a crossflow. *AIAA Journal*, **28**, 414–420.

[26] Humber, A.J., Grandmaison, E.W. and Pollard, A., 1993, Mixing between a sharp-edged rectangular jet and a transverse cross flow. *International Journal of Heat and Mass Transfer*, **36**, (18) 4307–4316.

[27] Lim, T.T., New, T.H. and Luo, S.C., 2001, On the development of large-scale structures of a jet normal to a cross flow. *Physics of Fluids*, **13**, (003), 770–775.

[28] Rosenhead, L., 1931, The formation of vortices from a surface of discontinuity. *Proceedings Royal Society London*, **A(134)**, 170–192.

[29] Rehbach, C., 1977, Calcul numérique d'écoulements tridimensionnels instationnaires avec nappes tourbillonnaires. *La Recherche Aérospatiale*, **5**.

[30] Leonard, A., 1980, Vortex methods for flow simulation. *Journal of Computational Physics*, **37**, 289–335.

[31] Mansour, N.N., Ferziger, J.H. and Reynolds, W.C., 1978, Large-eddy simulation of a turbulent mixing layer. Report TF-11, Thermosciences Divison, Department of Mech. Engineering, Stanford University.

[32] Cottet, G.H. and Koumoutsakos, P.D., 2000, *Vortex Method: Theory and Practice*, (Cambridge: Cambridge University Press).

[33] Koumoutsakos, P., 1997, Inviscid axisymmetrization of an elliptical vortex. *Journal of Computational Physics*, **138**, 821–857.

[34] Nitsche, M., 1992, Axisymmetric vortex sheet roll-up. Ph.D. thesis, University of Michigan.

[35] Chorin, A.J., 1973, Numerical study of slightly viscous flow. *Journal of Fluid Mechanics*, **57**.

[36] Degond P. and Mas-Gallic, S., 1989, The weighted particle method for convection-diffusion equations. *Mathmatics of Computationel*, **53**, 485–508.

[37] Choquin J.P. and Huberson, S., 1989, Particles simulation of viscous flow. *Computers and Fluids*, **17**, (2), 397–410.

[38] Degond, P. and Mustieles, F.J., 1990, A deterministic approximation of diffusion equations using particles. *SIAM Journal on Scientific and Statistical Computing*, **11**, 293–310.

[39] Rivoalen, E., Huberson, S. and Hauville, F., 1997, Numerical simulation of Navier Stokes equations by means of the particle method. *Comptes Rendus Academic Sciences*, Paris **324**(IIb), 543–549.

[40] Mansfield, J.R., Knio, O.M. and Meneveau, C., 1998, A dynamic LES scheme for the vorticity transport equation: formulation and a priori tests. *Journal of Computational Physics*, **145**(2), 693–730.

[41] Abramovich, G.N., 1963, *The Theory of Turbulent Jets* (The Massachuset Institute of Technologie).

[42] Dubief, Y. and Delcayre, F., 2000, On coherent-vortex identification in turbulence. *Journal of Turbulence*, **1**(011).